Synthesis and Electrochemistry of Li_3MnO_4: Mn in the +5 Oxidation State

Juliette A. Saint[a], Marca M. Doeff[a] and John Reed[b]

a) Materials Sciences Division

Lawrence Berkeley National Laboratory

University of California

Berkeley, CA 94720

and

b) Quantum Simulations Group

Lawrence Livermore National Laboratory

Livermore, CA 94550

Acknowledgment

This work was supported by: the Assistant Secretary for Energy Efficiency and Renewable Energy, Office of FreedomCAR and Vehicle Technologies of the U.S. Department of Energy under contract no. DE-AC02-05CH11231, support for J. R. under DE-AC02-05-CH11231, subcontract no. 6806960; the MRSEC Program of the National Science Foundation under award number DMR-02-13282 and by the Assistant Secretary for Energy Efficiency and Renewable Energy. Methodological developments that made this work possible have been supported by the Department of Energy under contract number DE-FG02-96ER45571. J.R. thanks Dr. Gerbrand Ceder for valuable advice and discussions during this work.

Abstract

Computational and experimental work directed at exploring the electrochemical properties of tetrahedrally coordinated Mn in the +5 oxidation state is presented. Specific capacities of nearly 700 mAh/g are predicted for the redox processes of Li_xMnO_4 complexes based on two two-phase reactions. One is topotactic extraction of Li from Li_3MnO_4 to form $LiMnO_4$ and the second is topotactic insertion of Li into Li_3MnO_4 to form Li_5MnO_4. In experiments, it is found that the redox behavior of Li_3MnO_4 is complicated by disproportionation of Mn^{5+} in solution to form Mn^{4+} and Mn^{7+} and by other irreversible processes; although an initial capacity of about 275 mAh/g in lithium cells was achieved. Strategies based on structural considerations to improve the electrochemical properties of MnO_4^{n-} complexes are given.

Keywords: Li_3MnO_4, Mn(V), MnO_4^{n-}, lithium ion battery

Introduction

The energy densities of lithium ion batteries are currently limited by the relatively low capacities of commercial positive electrode materials. These are typically layered metal oxides such as $LiCoO_2$, variants of $LiMn_2O_4$ spinels, or $LiFePO_4$. For the oxides, the maximum theoretical capacity is about 280 mAh/g and for the phosphates about 170 mAh/g, based on an average change of metal oxidation state of ±1. In vanadium oxides where multiple oxidation states for V are accessible, capacities are much higher, although practical considerations preclude use in a lithium ion configuration.

A study describing the electrochemistry of Li_2MnO_3 in a cell with a Li anode [1] reported that oxidation of Mn^{4+} to Mn^{5+} had occurred with concomitant extraction of Li. This would imply that it might be possible to exploit multiple oxidation states for Mn (e.g., from Mn^{3+} to Mn^{5+}) in some structures to achieve higher energy densities. Subsequent work [2] showed, however, that several complex processes take place during cell charge, including simultaneous loss of Li and oxygen from Li_2MnO_3, rather than simple oxidation of the metal.

This is not too surprising, because Mn^{5+} is rare, and is generally not octahedrally coordinated like Mn^{4+} in Li_2MnO_3. Rather, in compounds such as Li_3MnO_4, Mn^{5+} is usually tetrahedrally coordinated by oxygen [3]. The difficulty in oxidizing octahedrally coordinated Mn^{4+} (Mn^{4+}_{oct}) in Li_2MnO_3 to octahedral Mn^{5+} (Mn^{5+}_{oct}) can be readily understood with ligand field theory (LFT) [4, 5]. According to LFT, the splitting of the d-orbital energy levels by an octahedral field is, in general, substantially larger than that caused by the tetrahedral ligand field [6] (Figure 1a). Additionally, the structure of the octahedrally split levels is inverted relative to the tetrahedral splitting. The strong ligand

field splitting caused by octahedral coordination means that generally it is much harder to remove electrons from the low-lying t_{2g} levels of Mn^{4+}_{oct} to produce Mn^{5+}_{oct} than to remove electrons from the high-lying e_g levels when oxidizing Mn^{3+}_{oct} to Mn^{4+}_{oct}. As a result, while the oxidation of Mn^{3+}_{oct} to Mn^{4+}_{oct} occurs at accessible potentials, the oxidation of Mn^{4+}_{oct} to Mn^{5+}_{oct} is expected to occur at impractically high potentials (Figure 1b). This explains why it is generally not feasible to oxidize octahedrally coordinated Mn^{4+} to Mn^{5+}, and why octahedrally coordinated Mn^{5+} is rare or perhaps nonexistent.

In contrast, the ligand field splitting caused by tetrahedral coordination indicates that the oxidation of Mn^{4+}_{tet} to Mn^{5+}_{tet} should not be much more difficult than the oxidation of Mn^{3+}_{tet} to Mn^{4+}_{tet} as both processes remove electrons from the higher energy t_2 levels (Figure 1b). Furthermore, since all the *d* orbitals remain close in energy due to the relatively weak splitting caused by a tetrahedral ligand field (Figure 1a), even oxidations above Mn^{5+}_{tet}, which draw electrons from the lower *e* levels, are expected to be relatively close in potential to the $Mn^{3+/4+}$ redox couple, compared to the case with octahedral coordination. Consequently, LFT suggests that tetrahedral Mn could be practically oxidized all the way up to +7.

In keeping with this observation, a number of MnO_4^{n-} compounds are known to exist [7, 8, 9, 10, 11, 12, 13, 14] with oxidation states of Mn ranging from +2 to +7 (i.e., n ranging from 1-6). Examples are presented in Table 1 and several of the structures are illustrated in Figure 2. This suggests it might be possible to achieve high energy densities by exploiting multiple redox processes in compounds with MnO_4^{n-} oxyanions. For example, the theoretical capacity for conversion of antifluorite Li_6MnO_4 to $LiMnO_4$ (i.e.,

$Mn^{2+} \leftrightarrow Mn^{7+}$) is nearly 835 mAh/g. Of course, practical considerations may reduce utilization considerably; e.g., the high reactivity of permanganate with organic components in the cells is likely to result in irreversibility and safety problems. Additionally, Li_6MnO_4 shows little electrochemical activity in contrast to antifluorite structures containing other transition metals [7, 15]. However even if Mn is not reduced all the way to +2 as in the antifluorite structure, nearly 350 mAh/g should be attainable for the two electron process involved in reducing Li_3MnO_4 to Li_5MnO_4, and even another 200 mAh/g if oxidation is stopped at Li_2MnO_4, making investigation into the electrochemistry of this system worthwhile. Herein we describe experimental and computational work designed to determine if such processes are feasible in a lithium battery configuration.

Experimental

First-principles quantum mechanical calculations based on Density Functional Theory (DFT) [16, 17, 18] were performed using the Vienna Ab-Initio Simulation Package (VASP) [19]. The spin polarized generalized gradient approximation (GGA) [20, 21], Perdue-Wang exchange correlation function, and ultra-soft pseudopotentials were used [22]. Previous studies have found that various properties of *3d* transition metal oxides can be determined with good accuracy using DFT-based methods [23, 24, 25, 26]. Voltage calculations at 0K temperature for Mn oxide electrode materials and the determination of Mn oxidation state were performed following the procedures described in [27].

The process used to synthesize Li_3MnO_4 was very similar to the one developed by Kilroy et al. [28]. An intimately ground mixture of $LiOH \bullet H_2O$ and $LiMnO_4 \bullet 3H_2O$ in a

2:1 ratio was introduced into a furnace heated to 70°C under flowing oxygen. After equilibration, the sample was re-ground and the furnace temperature raised 10°C. This process was repeated for several increments of 10°C, up to 125°C. At this temperature, a gradual change in color from violet to blue occurs. After one hour at 125°C, heating was continued at 170°C for 2-3 hours. The final product is dark blue-green. During the heating procedure, the mixture was monitored by powder x-ray diffractometry (XRD) to check for unreacted $LiOH•H_2O$ and $LiMnO_4•3H_2O$, or signs of decomposition. If the mixture was heated too fast or if the temperature exceeded 170°C, the product turned brown and peak intensities in the XRD patterns decreased. Previous reports indicate that decomposition occurs above 200°C, close to the synthesis temperature, or when the powder is heated for a long time [29]. The product also turns brown when exposed to atmosphere for several days.

Lithium intercalation into Li_3MnO_4 was also performed by chemical reaction with *n*-butyl-lithium (1.6 M solution in hexane). The reaction was carried out in a glove box under helium atmosphere and at room temperature, the reaction time varying between 3 days and 1 week. The resulting black powders were washed with n-hexane and dried at room temperature for 3h under vacuum.

XRD patterns were acquired using a Philips X'Pert diffractometer equipped with an X'celerator detector using CuKα radiation (λ=1.54 Å). Theoretical patterns were constructed using the program Powdercell 2.4 by W. Kraus and G. Nolze (Federal Institute for Materials Research and Testing, Berlin, Germany). For quasi-*in situ* XRD experiments, fresh, discharged, and cycled electrodes were removed from coin cells and placed in a special gastight holder equipped with a Be window to avoid contact with air.

Electrodes were composed of 80 wt% active material, 8 wt% Kynar poly(vinylidene fluoride) (PVDF) (Elf Atochem North America Inc., Technical Polymers Department), 6 wt% SFG-6 synthetic flake graphite (Timcal Ltd., Graphites and Technologies), and 6 wt% acetylene black. Slurries of the mixture in 1-methyl-2-pyrrolidinone (Sigma Aldrich, 99%) were cast onto carbon coated aluminum current collectors (Intelicoat Technologies) and dried for 24 hours in air followed by 12-24 hours in a vacuum oven at 120 °C. Cathodes with an area of 1.8 cm^2 were punched from the cast electrode and typically had loadings of about 3-4 mg active material/cm^2. Assembly of lithium half-cells in 2032 coin cells was performed in a helium filled glove box using 1 M $LiPF_6$ in 1:2 ethylene carbonate/dimethylcarbonate (EC/DMC) electrolyte solution and a Celgard 3401 separator. Potentiostatic and galvanostatic experiments were carried out on a Macpile II (Bio-Logic, S.A., Claix, France) automated cycling data recorder. For potentiostatic experiments, 10 mV steps were taken between set voltage limits, with each new step initiated after the current had decayed to 0.025 mA.

Results and Discussion

Ab initio potential calculations at T=0K were performed on several types of Mn oxide systems, some of which are hypothetical. These are:

1) α-$NaFeO_2$-type layered structures with octahedrally coordinated Mn:

a) The metastable $LiMnO_2$ structure [30, 31, 32, 33, 34].

b) The experimentally known Li_2MnO_3 structure in which layers of pure Li alternate with those containing 2/3 Mn and 1/3 Li [35].

c) A hypothetical $Li_2[Al_{1/2}Mn_{1/2}]O_3$ structure similar to 1b, in which half of the Mn is replaced with Al.

2) Hypothetical analogs to 1a, b, and c where both Mn and Li are tetrahedrally coordinated.

The hypothetical type 2 structures can be envisioned by uniformly shifting all the cations in the type 1 structures from octahedral sites to neighboring tetrahedral sites within the fixed cubic close-packed oxygen framework. The configuration of cations relative to one another is the same in both structure types; i.e., alternating close packed (111) planes of Li and M (where M=Mn, 2/3Mn + 1/3Li, or 1/3Mn+1/3Li+1/3Al). The only difference is the oxygen coordination of these cations (either all octahedral or all tetrahedral).

For each of the structures, the average potential and Mn oxidation state at 0K was calculated for both fully lithiated and fully delithiated versions, where Li is removed only from the lithium layer (Table 2). Note that DFT/GGA potential calculations on transition metal oxides are found to be systematically low compared to reported experimental values [27, 36]. For example, layered $LiMnO_2$ discharges at an average potential of about 3.5V vs. Li [30], but a potential of 2.7V is calculated using DFT with GGA. Since the underestimation is systematic, actual potentials can be expected to be about 0.5-0.8V higher than the calculated values presented in this study.

As predicted by LFT, Table 2 indicates that the steps in potential are greater for octahedral Mn than for tetrahedral Mn. For example, the +5/+7 redox couple for octahedral Mn, in which electrons are removed from the t_{2g} orbitals, is 1.8V above that for +3/+4, in which an electron is removed from an e_g orbital (Figure 1b). The difference is only 0.5V for tetrahedral Mn between the +5/+7 redox couple where electrons are

removed from *e* orbitals and the +3/+4 redox couple where electrons are removed from a t_2 orbital (Figure 1b).

The average potentials for the tetrahedral Mn +3/+4, +4/+6, and +5/+7 redox couples falls between those for octahedral Mn +3/+4 and +4/+6 ones, indicating that the tetrahedral *d* levels lie between the split octahedral *d* levels t_{2g} and e_g in energy. This has been found to be true for a wide variety of manganese oxide structures and compositions [26, 37].

Table 2 suggests that a number of redox states for tetrahedral Mn are accessible at potentials compatible with lithium battery operations, which could lead to very high energy densities. While it is doubtful that layered structures with tetrahedral Mn such as those listed in Table 3 could be readily synthesized due to the general preference of Mn for octahedral coordination in many oxidation states, MnO_4^{n-} complexes are known for a wide range of n (Tab1e 1 and Figure 2).

To investigate the properties of MnO_4^{n-} oxyanionic complexes, first principle calculations were performed on a lithium-containing analog of the Na_5MnO_4 structure shown in Figure 2, where Mn is initially in the +3 oxidation state. The delithiation is predicted to occur topotactically (e.g., the framework of MnO_4^{n-} tetrahedra is maintained) via two two-phase reactions as follows:

1) $$Li_5MnO_4 \underset{+2Li^+,+2e^-}{\overset{-2Li^+,-2e^-}{\rightleftarrows}} Li_3MnO_4 \qquad (1.9V \text{ vs. } Li)$$

2) $$Li_3MnO_4 \underset{+2Li^+,+2e^-}{\overset{-2Li^+,-2e^-}{\rightleftharpoons}} LiMnO_4 \qquad (3.4V \text{ vs. Li})$$

These processes yield a total theoretical capacity of 698 mAh/g. Ball and stick representations of the calculated structures of the metastable $LiMnO_4$, Li_3MnO_4, and Li_5MnO_4 compounds are shown in Figure 3.

The relatively large split between the potentials in steps 1 and 2 is at odds with the data in Table 2 for tetrahedral Mn in a hypothetical layered structure, for which only a 0.5 V difference between the Mn^{7+}/Mn^{5+} and Mn^{4+}/Mn^{3+} redox couples was calculated. In the Li_xMnO_4 system, the $Mn^{5+}{}_{tet}/Mn^{3+}{}_{tet}$ redox couple is affected by cationic crowding (i.e., there are three cations for every two oxygen anions in Li_5MnO_4). A similar effect of cationic crowding is also observed in the experimentally known hexagonally close-packed structure $Li_2Mn_{oct}O_2$ [38], which has a 3:2 cation to oxygen ratio. For this compound, a potential of only 1V is calculated for the $Mn^{3+}{}_{oct}/Mn^{2+}{}_{oct}$ couple. This is 1.7 V lower than the potential of the layered $Mn_{oct}{}^{4+}/Mn_{oct}{}^{3+}$ couple, even though the Fermi level lies in the e_g band for both redox couples. These results suggest that, beyond a certain point, cation crowding has an impact on the voltage that outweighs the ligand field effects.

To examine further the electrochemistry of the $MnO_4{}^{n-}$ system, Li_3MnO_4 was synthesized. Figure 4 shows the XRD powder pattern obtained on the dark blue-green powder synthesized as described above. This most closely matches that calculated for α-Li_3MnO_4 (the low temperature form) using the cell parameters reported in reference [3] and atom positions for Li_3VO_4, substituting Mn for V (Table 3). The patterns predicted

for α-Li_3MnO_4 and β-Li_3MnO_4 (Li_3PO_4 structure-type) are similar, distinguishable mainly by the presence of an extra peak (121) at 2θ=34.82°, for the latter. The powder hydrolyzes slowly upon exposure to moist air, but is stable upon storage for at least four months under an inert atmosphere. When water is added in the presence of air, it reacts to form a brown precipitate and a purple solution, indicative of permanganate ion. All peaks in the XRD pattern obtained on the dried product could be indexed to either Li_2CO_3 or $LiMnO_4 \bullet 3H_2O$. This suggests that the brown precipitate is an amorphous form of MnO_2. The reaction is consistent with the following disproportionation scheme:

(3) $$3Mn^{5+}(aq.) \rightarrow Mn^{7+}(aq.) + 2Mn^{4+}\downarrow$$

Addition of n-butyllithium to Li_3MnO_4 caused the blue-green powder to turn black. XRD powder patterns taken on the products after three days or six days of reaction time are shown in Figure 5. There is considerable broadening and shifting of the peaks belonging to the original Li_3MnO_4 phase, as well as the appearance of several new weak reflections at 2θ=18.2°, 19.94°, and 20.4° (most evident after six days of reaction) and a strong one at 44.3°, observed in both patterns. This indicates that a new phase is slowly formed upon chemical reduction with n-butyllithium.

Li/Li_3MnO_4 cells have an open circuit potential of about 3.4V. Cells can be either charged or discharged initially, although rate limitations are evident in galvanostatic experiments. Differential capacity plots derived from stepped potential experiments where voltage limits were varied, are shown in Figure 6 a-d. A reversible broad feature centered near 3V is observed in all the plots. When the potential is stepped down to 2.0V (Figure 6b), a very sharp and intense peak is observed near the end of discharge. Although it recurs upon the second cycle, it is not reversible; no analogous

feature is seen during the subsequent charge. This suggests that the material is not fully utilized during the first reduction under these conditions. Upon discharge to lower potentials (Figure 6c), the feature centered near 2.0V is apparent only upon the first discharge, confirming this. It is replaced by a broad, quasi-reversible set of peaks centered near 1.8V upon the second and subsequent cycles. A sharp, irreversible peak near the end of charge, which is repeated upon subsequent cycles, is also seen in the cell stepped to 4.4V in Figure 6d. The reversible feature near 3V and the irreversible ones near 2.0 and 4.4V are observed regardless of whether cells are discharged first or charged (not shown).

The initial range of composition for the $Li_{3\pm x}MnO_4$ electrode is shown in Figure 7, which combines voltage profiles from two different cells charged or discharged galvanostatically at low current densities. Although the total specific capacity spanned by these two cells is more than 275 mAh/g, the composition range is still smaller than expected. Approximately 0.5 Li per Li_3MnO_4 can be extracted upon charge to 4.5V to yield "$Li_{2.56}MnO_4$" and 1 Li can be inserted upon discharge to give "Li_4MnO_4" under these conditions, rather than the expected end-members $LiMnO_4$ and Li_5MnO_4. The observed capacities of Li/Li_3MnO_4 cells, however, are a strong function of the discharge or charge current density, indicating severe rate limitations. This is not too surprising, considering that these ionic solids are expected to have very low electronic conductivity.

The voltage profiles of cells cycled galvanostatically change after the first cycle. After the initial conversion, however, the cycling behavior is fairly stable, with sloping discharge profiles centered at about 3.1V (Figure 8). The capacities achieved upon

cycling are dependent upon the history of the cell, but are generally much lower than that found initially.

The electrochemical characteristics of Li_3MnO_4 indicate that both the initial insertion and extraction of Li from the structure are not reversible. In order to obtain further insights, a quasi-*in situ* XRD experiment, for which fresh, discharged, and cycled electrodes were removed from coin cells and placed in a sealed holder with a Be window, was carried out. Figure 9 shows the low angle patterns (where cell and holder components do not interfere) obtained on the three types of electrodes. While reflections attributable to the Li_3MnO_4 phase are clearly visible in the pattern of the fresh electrode, these have disappeared from the patterns of the discharged and charged electrodes and are replaced by an extremely broad peak centered around $2\theta=23°$. In addition, new broad reflections at about $2\theta=15.1°$, 17.95° and 19.4° are observed for these electrodes. The latter three approximately match the positions of the new reflections seen in the pattern of the product obtained by chemical reduction (Figure 5). These results indicate that Li insertion results in the destruction of the Li_3MnO_4 structure. A new phase is formed, although there is not enough information to determine the identity of this product or ascertain whether it is electroactive.

The irreversibility accounts for the fact that the electrochemical features of the Li_3MnO_4 electrode do not match the predicted potentials, even taking in account the systematic under-estimation of the DFT calculations. The values given in equations (1) and (2) assume topotactic insertion and extraction of Li from a structure analogous to Na_5MnO_4 in Figure 2. However, the Li_3MnO_4 that is formed by removing ions from the 4b sites in "Li_5MnO_4" does not have the same structure as synthesized α-Li_3MnO_4,

although the space group assignments are the same. This is readily apparent when comparing the polyhedral views of the hypothetical Li_3MnO_4 with that of α-Li_3MnO_4. The Li_3MnO_4 used in the DFT calculations and shown in Figure 10a contains unconnected MnO_4 tetrahedra lying in the same plane. They share corners with NaO_4 tetrahedra above and below the plane. The NaO_4 tetrahedra in turn are linked to one another via edges and corners to form layers. The empty 4b sites between the Mn tetrahedra readily accommodate insertion of ions to yield the Na_5MnO_4 structure shown in Figures 2 and 3. In contrast, the oxygen array in α-Li_3MnO_4 is hexagonally close-packed so that LiO_4 and MnO_4 tetrahedra share all corners with one another (Figures 2 and 10b). Insertion of Li into empty sites then requires cation occupied tetrahedra to share faces. This is energetically unfavorable, so reductive insertion of Li destroys the structure, resulting in the irreversibility evident in the stepped potential experiments shown in Figure 6. Removal of Li likewise may result in structural instability for this compound. As an aside, it should be noted that removal of Li from either the hypothetical Li_3MnO_4 shown in Figure 10a or α-Li_3MnO_4 will not result in the experimentally found $LiMnO_4$ structure shown in Figure 2, where Li is in octahedral coordination.

The computational approach used herein has not been applied to the prediction of potentials for irreversible processes such as those seen during the electrochemical cycling of α-Li_3MnO_4. However, the electrochemical feature near 3V in Li/Li_3MnO_4 cells appears to be reversible and is not consistent with tetrahedral Mn according to DFT. Instead this is characteristic of the redox processes of octahedrally coordinated $Mn^{3+/4+}$ (Table 2). Because this feature is present before significant oxidation or reduction has

occurred (e.g., see Figure 6a) it suggests that it is not merely due to a subsequent product of one of these irreversible processes. During cell assembly, however, a purple coloration of the electrolytic solution was sometimes observed after it was added to the Li_3MnO_4 cathode. This is evidence of partial dissolution of the active material and subsequent disproportionation (equation 3) to form permanganate and amorphous MnO_2. The XRD patterns of Li_3MnO_4 electrodes wet by the electrolytic solution appear unchanged compared to dry electrodes except for an extremely broad background peak, which may belong to the amorphous component. It is most likely this component that gives rise to the observed initial reversible electrochemical activity near 3V. The specific capacity associated with this redox process is fairly low (about 50 mAh/g, although there is some variability) suggesting only a small amount of the Li_3MnO_4 undergoes the disproportionation reaction. This is supported by the fact that the peaks attributable to Li_3MnO_4 in wetted electrodes are still quite strong and do not appear to be broadened by (for example) particle size diminution. Thus, it is reasonable to assume that the other electrochemical processes discussed above are attributable to Li_3MnO_4 and specifically redox processes involving tetrahedral Mn^{5+}, not the products of the disproportionation reaction.

The reversibility of electrodes based on tetrahedrally coordinated Mn can be improved by selection of structures more amenable to lithium insertion and extraction processes, as discussed above. This may be achieved, for example, by preparation of a metastable Li_3MnO_4 compound via ion-exchange and controlled oxidation of the Na_5MnO_4 shown in Figure 2, rather than using either directly synthesized α- or β-Li_3MnO_4. Development of alternative electrolytic solutions may minimize the

dissolution/disproportionation processes, which evidently result in decomposition and electrochemical properties inferior to those predicted by computational methods. Another problem remains: that of the poor electronic conductivity implied by the salt-like structures of materials with MnO_4^{n-} oxyanions, which impacts rate capability. This may be ameliorated via carbon-coating techniques, as has been done with $LiFePO_4$ [39], or by partial substitution of Li with a transition metal. For example, replacement of 1/5 of the Li in Li_5MnO_4 with Cu to give Li_4CuMnO_4 improves the ratio of transition metal to oxygen to 1:2, as is found in $LiMn_2O_4$. The theoretical capacity, based on removal of all Li and no contribution from Cu, is reduced somewhat, but is still a very high 510 mAh/g. There is even less impact on the theoretical capacity if only 1/10 of the Li is substituted to give $Li_9Cu(MnO_4)_2$, for a total of 590 mAh/g. First principles calculations predict similar two-phase electrochemical behavior for the substituted materials as for Li_xMnO_4, with potentials at 3.0 and 2.1V for Li_4CuMnO_4 and 3.3 and 1.8V for $Li_9Cu(MnO_4)_2$. The calculations indicate that Cu^{+1} coexists with Mn^{7+} in these systems. This provides an additional example of the relatively weak oxidation strength of tetrahedral $Mn^{5+/7+}$ compared to octahedral Mn in the same oxidation states. Calculations for materials with octahedrally coordinated Mn coexisting with Cu in cubic close-packed oxides indicate that Cu should generally be oxidized above +1 when the Mn oxidation state goes above +4 [26, 37].

In keeping with these observations, it is interesting to note the existence of tetrahedrally coordinated Mn oxyanions in phosphate and vanadate hosts [40, 41]. The presence of PO_4^{3-} or VO_4^{3-} groups may stabilize Mn^{5+} sufficiently to discourage disproportionation in solution. Replacement of MnO_4^{n-} groups with PO_4^{3-} will reduce

specific capacity, so mixed MnO_4^{n-}-VO_4^{3-} compounds are preferred. Finally, electronic conductivity may be improved by the presence of the metal in VO_4^{3-} groups in mixed metal oxyanion complexes.

Conclusions

The possibility of exploiting multiple oxidation states in MnO_4^{n-} oxyanionic complexes to obtain very high specific capacities is discussed. First principles calculations predict two two-phase regions in the voltage profiles of Li/Li_xMnO_4 cells. Extraction of Li from Li_3MnO_4 to form $LiMnO_4$ should occur at about 3.4V and insertion of Li into Li_3MnO_4 to form Li_5MnO_4 should occur at approximately 1.9V for a total theoretical capacity of 698 mAh/g. In practice, synthesized α-Li_3MnO_4 yields much lower capacities and exhibits several irreversible electrochemical features due to its structure. In addition, disproportionation of Mn^{5+} into Mn^{7+} and Mn^{4+} complicates the electrochemical behavior. Several suggestions to improve the reversibility and to ameliorate the disproportionation are given.

Acknowledgment

This work was supported by: the Assistant Secretary for Energy Efficiency and Renewable Energy, Office of FreedomCAR and Vehicle Technologies of the U.S. Department of Energy under contract no. DE-AC02-05CH11231, support for J. R. under DE-AC02-05-CH11231, subcontract no. 6806960; the MRSEC Program of the National Science Foundation under award number DMR-02-13282 and by the Assistant Secretary for Energy Efficiency and Renewable Energy. Methodological developments that made this work possible have been supported by the Department of Energy under contract

number DE-FG02-96ER45571. J.R. thanks Dr. Gerbrand Ceder for valuable advice and discussions during this work.

References

1. P. Kalyani, S. Chitra, T. Mohan, S. Gopukumar, J. Power Sources 80 (1999) 103-106.

2. A. D. Robertson, P.G. Bruce, Chem. Mater. 15 (2003) 1984-1992.

3. G. Meyer, R. Hoppe, Z. Anorg. Allg. Chem. 424 (1976) 249-256.

4. R.G. Burns, Mineralogical Applications of Crystal Field Theory, Cambridge University Press (1970, 1993), p.17.

5. B.N. Figgis, M.A. Hitchman, Ligand Field Theory and its Applications, Wiley-VCH (2000), p.116.

6. R.G. Burns, Mineralogical Applications of Crystal Field Theory, Cambridge University Press, (1970, 1993), p. 22.

7. S. Narukawa, Y. Takeda, M. Nishijima, N. Imanishi, O. Yamamoto, M. Tabuchi, Solid State Ionics 122 (1999) 59-64.

8. G. Brachtel, N. Bukovec, R. Hoppe, Z. Anorg. Allg. Chem. 515 (1984) 101-113.

9. R. Olazcuaga, J.-M. Reau, M. Devalette, G. Le Flem, P. Hagenmuller, J. Solid State Chem. 13 (1975) 275-282.

10. Z. Gontarz, R. Grzybowska, R. Sabalinski J. Thermal Anal. 45 (1995) 1125-1133.

11. R. Olazcuaga, G. Le Flem, P. Hagenmuller, Revue de Chim. Minerale 13 (1976) 9-23.

12. R. Scholder, U. Protzer Z. Anorg. Allg. Chem. 369 (1969) 313-326.

13. F. H. Herbstein, Acta Cryst. 13 (1960) 357.

14. D. Fischer, R. Hoppe, W. Schäfer, K. S. Knight, Z. Anorg. Allg. Chem. 619 (1993) 1419-1425.

15. A. Hirano, T. Matsumura, M. Ueda, N. Imanishi, Y. Takeda, M. Tabuchi, Solid State Ionics 176 (2005) 2777-2782.

16. R.G. Parr, W. Yang, Density-Functional Theory of Atoms and Molecules, Oxford University Press, New York (1989), pp. 51-52.

17. R.G. Parr, W. Yang, Density-Functional Theory of Atoms and Molecules, Oxford University Press, New York (1989), pp. 142-145.

18. K. Ohno, K. Esfarjani, Y. Kawazoe, Computational Materials Science, , Springer-Verlag, Berlin Heidelberg (1999) pp. 21-25.

19. G. Kresse, J. Furthmuller, Phys. Rev. B 54 (1996) 11169-11186.

20. R.G. Parr, W. Yang, Density-Functional Theory of Atoms and Molecules, Oxford University Press, New York (1989) pp. 153-154.

21. K. Ohno, K. Esfarjani, Y. Kawazoe, Computational Materials Science, Springer-Verlag, Berlin Heidelberg (1999) pp. 106-107.

22. D. Vanderbilt, Phys. Rev. B 41 (1990) 7892-7895.

23. G. Ceder, A. Van der Ven, Electrochim. Acta 45 (1999) 131-150.

24. S. K. Mishra, G. Ceder, Phys. Rev. B 59 (1999) 6120-6130.

25. A. Van der Ven, M.K. Aydinol, G. Ceder, J. Electrochem. Soc. 145 (1998) 2148-2155.

26. J. Reed, Ab-Initio Study of Cathode Materials for Lithium Batteries, PhD Thesis (2003) Massachusetts Institute of Technology.

27. J. Reed, G. Ceder, Electrochem. Sol. State Lett. 5 (2002) A145-A148.

28. W. P. Kilroy, S. Dallek, J. Zaykoski, J. Power Sources, 105 (2002) 75-81.

29. R. Scholder, D. Fischer, H. Waterstradt, Z. Anorg. Allg. Chem. 277 (1954) 234-248.

30. A. R. Armstrong, P.G. Bruce, Nature 381 (1996) 499-500.

31. F. Capitaine, P. Gravereau, C. Delmas, Solid State Ionics 89 (1996) 197-202.

32. A. Armstrong, A. Robertson, P. Bruce, Electrochim. Acta 45 (1999) 285-294.

33. P. Bruce, A. Armstrong, R. Gitzendanner, J. Mat. Chem. 9 (1999) 193-199.

34. Y. Shao-Horn, S. A. Hackney, A.R. Armstrong, P.G. Bruce, R. Gitzendanner, C. S. Johnson, M. M. Thackeray, J. Electrochem. Soc. 146 (1999) 2404-2412.

35. M. M. Thackeray, Prog. Solid State Chem. 25 (1997) 1-71.

36. M. K. Aydinol, A. F. Kohan, G. Ceder, K. Cho, J. Joannopoulos, Phys. Rev. B (Condensed Matter) 56 (1997) 1354-1365.

37. J. Reed, G. Ceder, Chem. Rev. 104 (2004) 4513-4534.

38. C. S. Johnson, J.-S. Kim, A. J. Kropf, A. J. Kahaian, J. T. Vaughey, L. M. L. Fransson, K. Edstrom, M. M. Thackeray, Chem. Mater. 15 (2003) 2313-2322.

39. J.D. Wilcox, M. M. Doeff, M. Marcinek, R. Kostecki, J. Electrochem. Soc. 154 (2007) A389-A395.

40. J. B. Milstein, J. Ackerman, S. L. Holt, B.R. McGarvey, Inorg. Chem. 11 (1972) 1178-1184.

41. K. M. S. Etheredge, A. S. Gardberg, S-J Hwu, Inorg. Chem. 35 (1996) 6358-6361.

Figure Captions

Figure 1. (a) Energy levels of the d-orbitals in octahedral and tetrahedral coordination. For convenience, the energy barycenter is depicted as the same, although it may not be for the two types of coordination. (b) Electron occupancy of the d-orbitals for Mn^{4+} ions in octahedral and tetrahedral coordination, showing removal of one electron to form Mn^{5+}. The Fermi level of Li is shown as a reference.

Figure 2. Structures of compounds containing MnO_4^{n-} anions, as indicated. MnO_4^{n-} tetrahedra are shaded dark gray and alkali metal containing polyhedra are light.

Figure 3. Hypothetical structures of Li_5MnO_4 (lithiated analog to Na_5MnO_4) Li_3MnO_4, and $LiMnO_4$, resulting from electrochemical de-intercalation of Li.

Figure 4. Calculated and experimental XRD powder patterns for α-Li_3MnO_4. Peaks attributable to aluminum from the sample holder are marked. Major reflections are indexed.

Figure 5. XRD powder patterns for Li_3MnO_4 powder (bottom) and the reaction product of Li_3MnO_4 with n-butyllithium after 3 days (middle) and 6 days (top). Reflections attributable to a new phase are indicated with arrows, and those for Li_2CO_3 are marked with asterisks. Al from the sample holder is also marked.

Figure 6. Differential capacity plots from stepped potential experiments on Li/Li_3MnO_4 cells: a) 2.3-3.5V, 7 cycles, b) 2.0-3.5V, 2 cycles, c) 1.8-3.5V, 5 cycles, and d) 2.3-4.4V, 5 cycles. First cycles are represented with dotted lines and subsequent cycles with solid lines. All cells were discharged initially.

Figure 7. Voltage profiles for two Li/Li_3MnO_4 cells discharged and charged at 0.014 mA/cm^2, showing the cumulative specific capacity.

Figure 8. Discharges of a Li/Li_3MnO_4 cell between 4.4 and 2.0V at 0.017 mA/cm^2. The cell was discharged initially.

Figure 9. Quasi-*in situ* XRD powder patterns obtained on a fresh electrode, one discharged to 1.8V and another one discharged and charged to 3.5V. Reflections not attributable to the original Li_3MnO_4 phase are marked with arrows. The theoretical pattern for α-Li_3MnO_4 is included.

Figure 10. (a) Polyhedral view of a hypothetical Li_3MnO_4 obtained by removing Li in 4b sites from a Li_5MnO_4 analog to Na_5MnO_4, shown in Figures 2 and 3. **(b)** actual structure of Li_3MnO_4. Mn tetrahedra are shaded dark, and alkali metal containing tetrahedra are light.

Table 1. Compounds containing MnO_4^{n-} Oxyanions

Compound	*Mn Ox. State*	*Space Group*	*Structure Type*	*Reference*
Li_6MnO_4	+2	$P4_2/nmc$	antifluorite	7
Na_5MnO_4	+3	$Pmn2_1$		8, 10
Na_4MnO_4	+4	$P\bar{1}$	Na_4SiO_4	9
α-Li_3MnO_4 (LT)	+5	$Pmn2_1$	wurtzite	3
β-Li_3MnO_4 (HT)	+5	Pnma	Li_3PO_4	3
K_2MnO_4	+6	Pnma		13
$LiMnO_4$	+7	Cmcm	β-CrO_4	14

Table 2. Calculated Potentials for Several Known and Hypothetical Lithium Manganese Oxide Structures

Composition and Structure	*Mn Redox Couple*	*Potential vs. Li (V)*
$LiMn_{oct}O_2$	$4^+ \leftrightarrow 3^+$	2.7
$LiMn_{tet}O_2$	$4^+ \leftrightarrow 3^+$	3.4
$Li_2Mn_{oct}O_3$	$6^+ \leftrightarrow 4^+$	4.4
$Li_2Mn_{tet}O_3$	$6^+ \leftrightarrow 4^+$	3.8
$Li_2[Al_{1/2}Mn_{1/2}]_{oct}O_3$	$7^+ \leftrightarrow 5^+$	4.5
$Li_2[Al_{1/2}Mn_{1/2}]_{tet}O_3$	$7^+ \leftrightarrow 5^+$	3.9

Table 3. Structural Parameters for α-Li_3MnO_4

Space group $Pmn2_1$: a=6.316 Å, b=5.429 Å, c=4.9400 Å

Atom	*Site*	*x*	*y*	*z*
Li1	4b	0.247	0.3315	0.9872
Li2	2a	0	0.8326	0.9848
Mn	2a	0	0.8291	1
O1	4b	0.2239	0.6804	0.8910
O2	2a	0	0.1296	0.8952
O3	2a	0	0.1736	0.8478

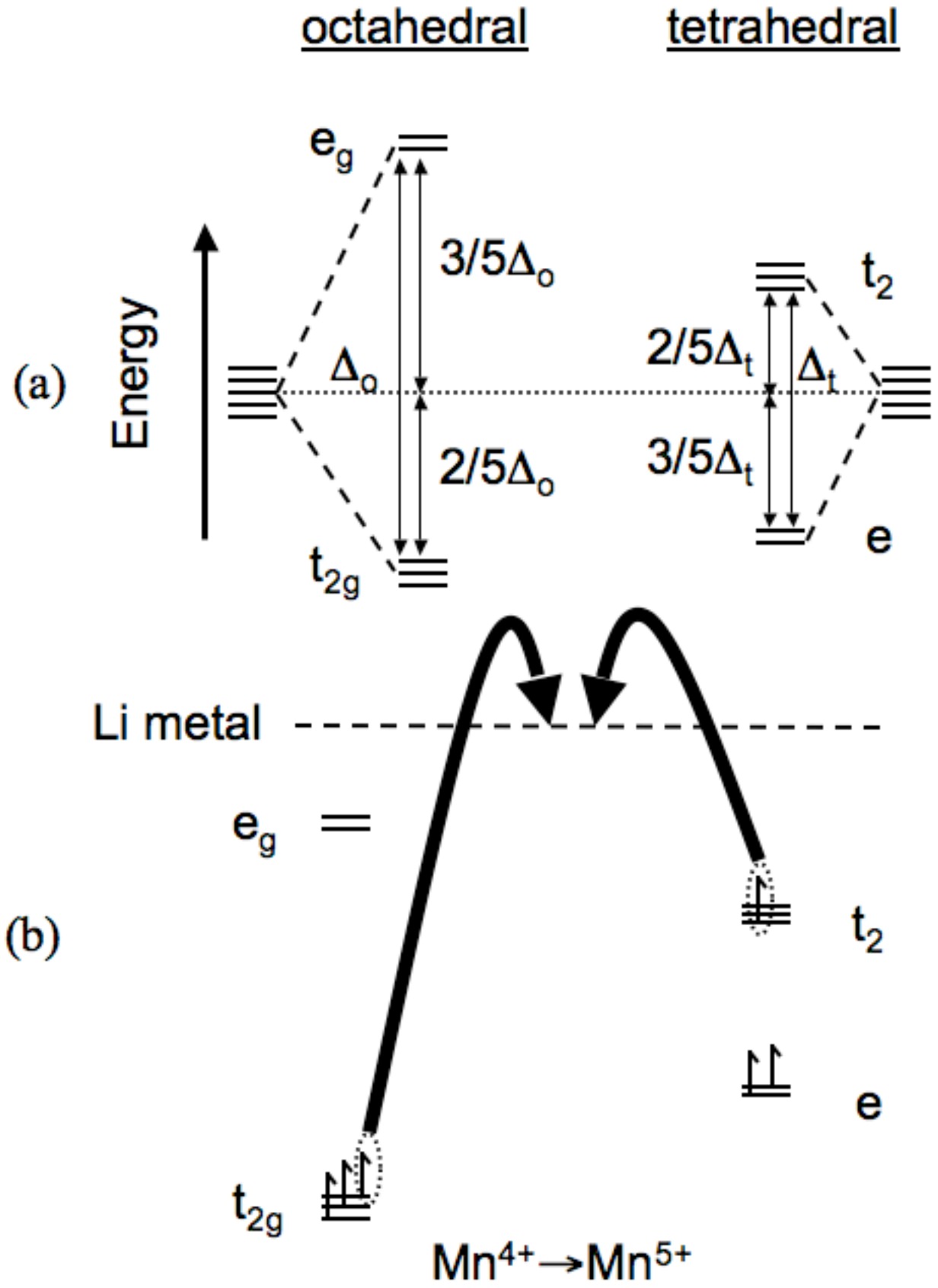
octahedral
tetrahedral
(a)
Energy
e_g
$3/5\Delta_o$
Δ_o
$2/5\Delta_o$
t_{2g}
t_2
$2/5\Delta_t$
Δ_t
$3/5\Delta_t$
e
(b)
Li metal
e_g
t_2
e
t_{2g}
$Mn^{4+} \rightarrow Mn^{5+}$

Figure 1

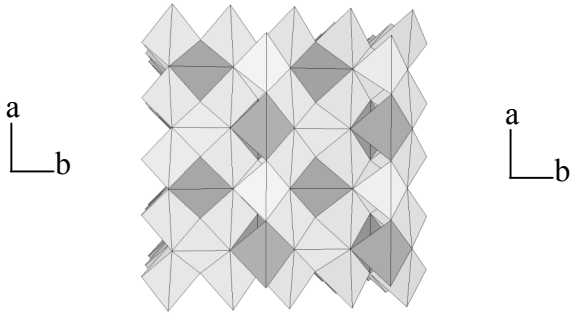

Li_6MnO_4 (antifluorite)

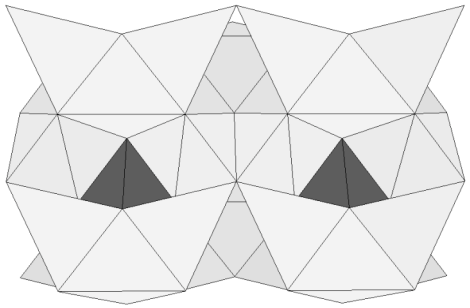

Na_5MnO_4

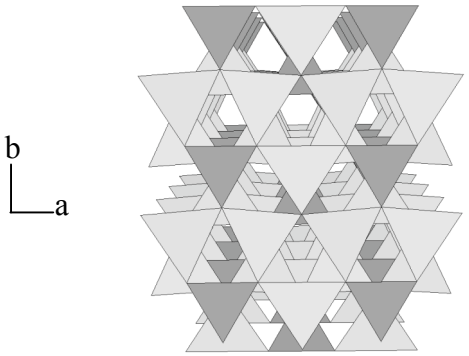

α-Li_3MnO_4 (wurtzite)

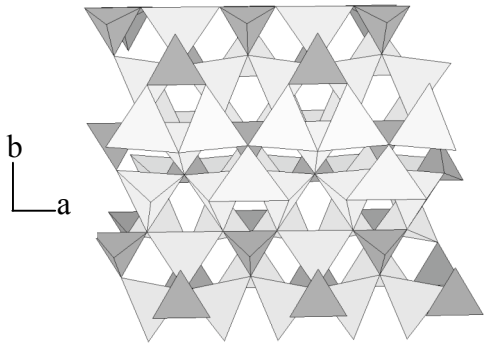

β-Li_3MnO_4 (Li_3PO_4-type)

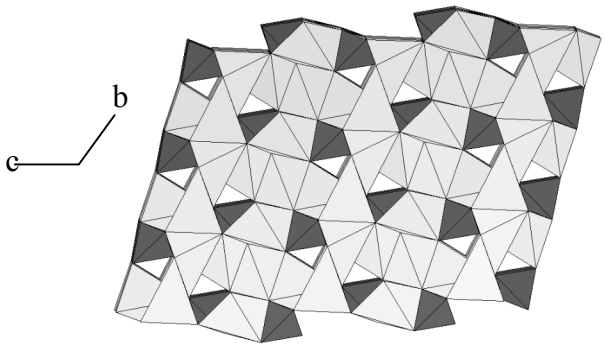

Na_4MnO_4

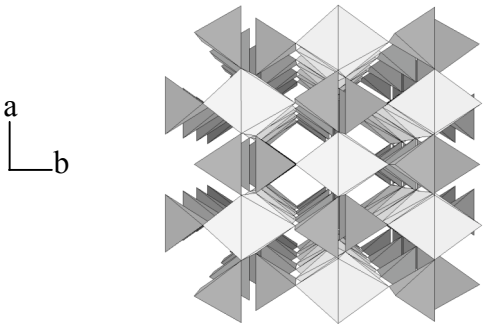

$LiMnO_4$ (β-$CrPO_4$-type)

Figure 2

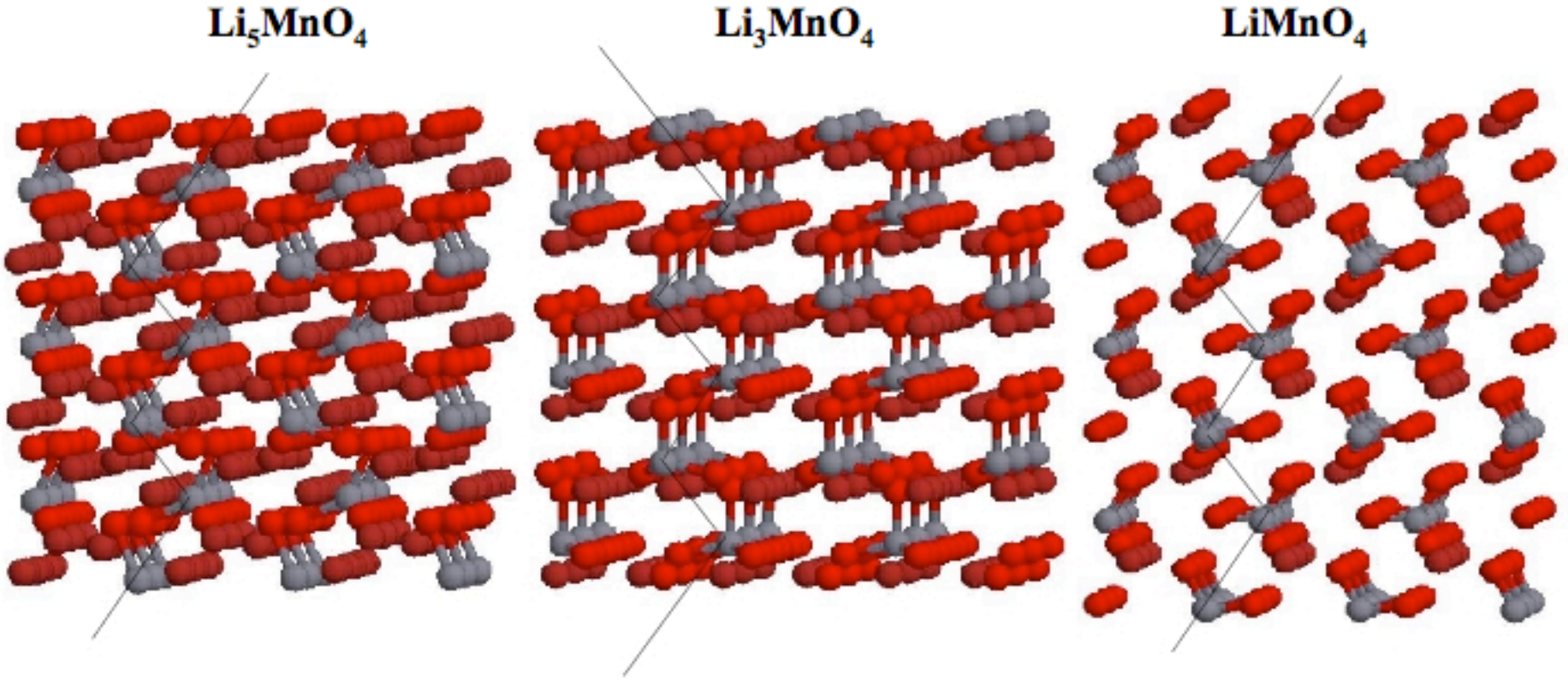

Figure 3

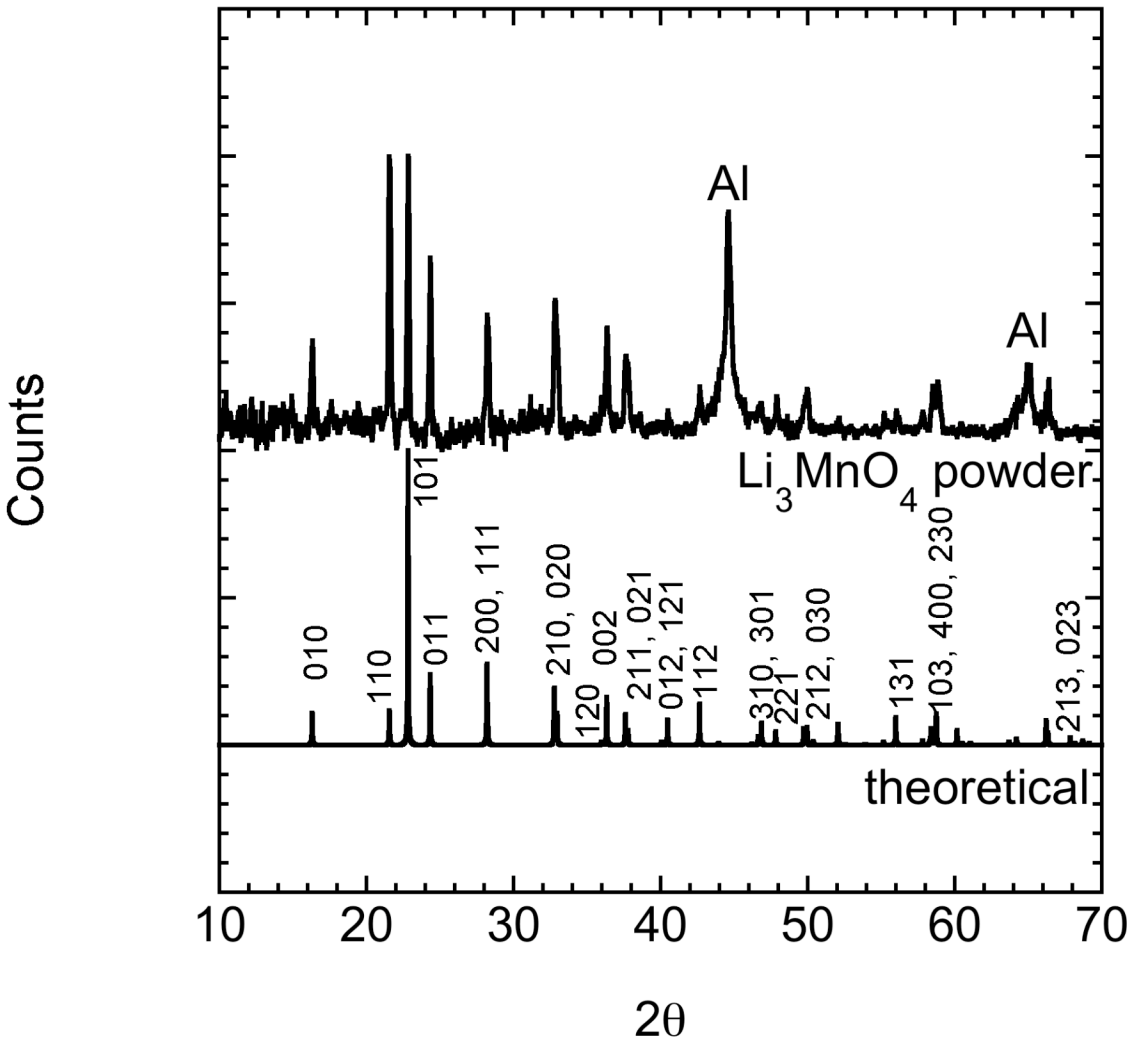
Counts
Al
Al
Li3MnO4 powder
101
010
110
011
200, 111
210, 020
002
120
211, 021
012, 121
112
310, 301
221
212, 030
131
103, 400, 230
213, 023
theoretical
10
20
30
40
50
60
70
2θ

Figure 4

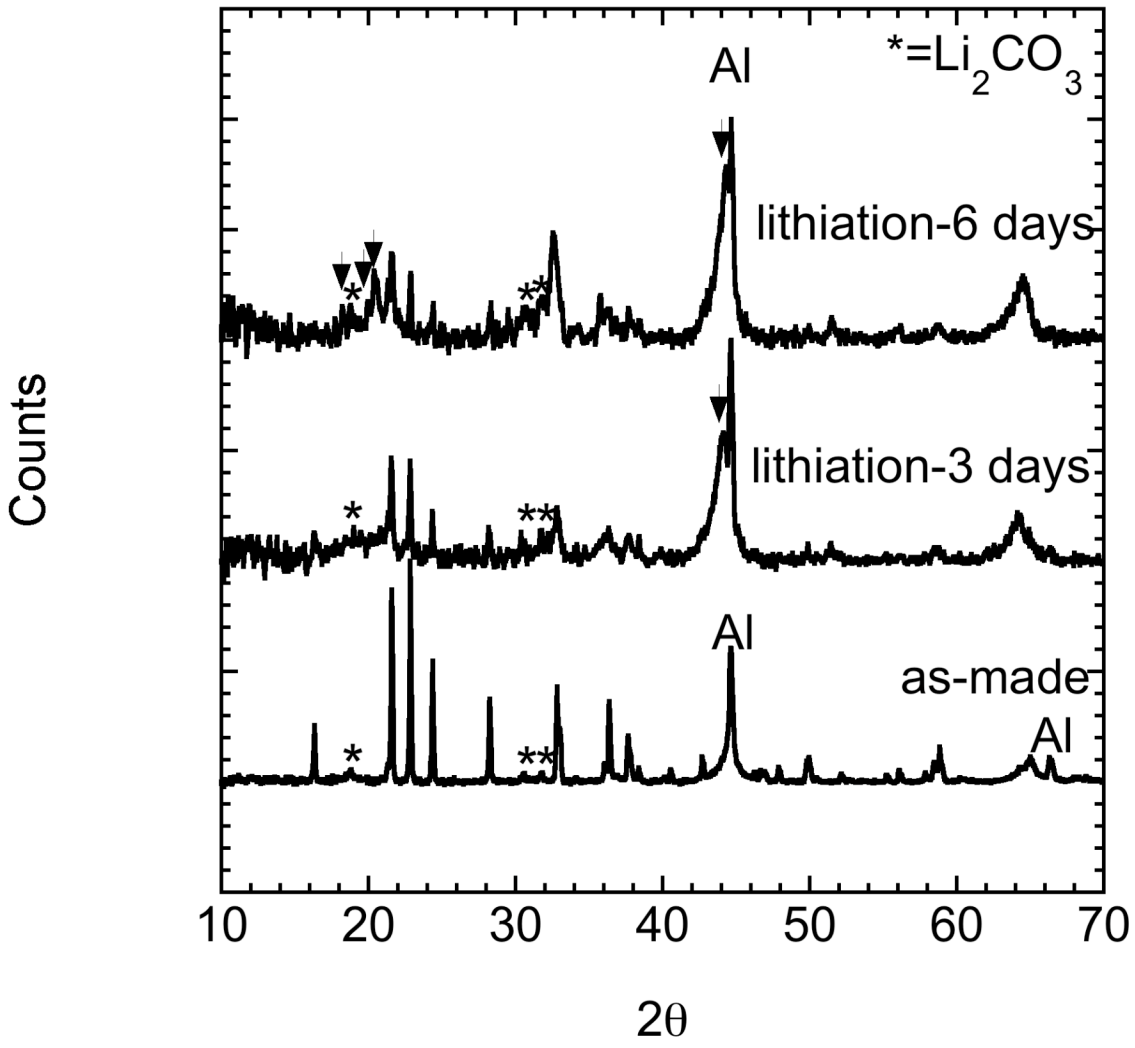
*=Li2CO3
Al
lithiation-6 days
lithiation-3 days
as-made
Al
Al
*
**
Counts
10
20
30
40
50
60
70
2θ

Figure 5

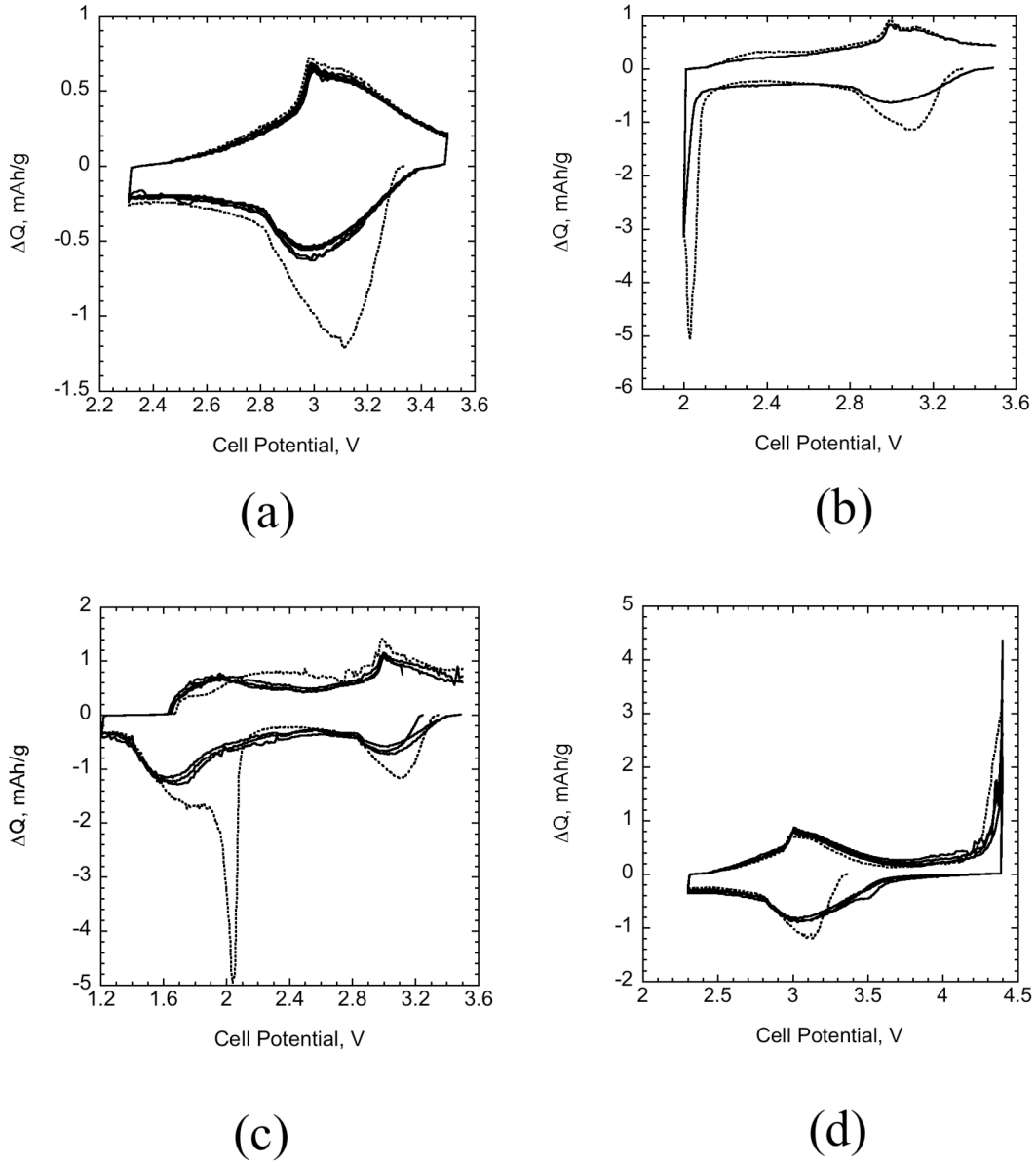

Figure 6

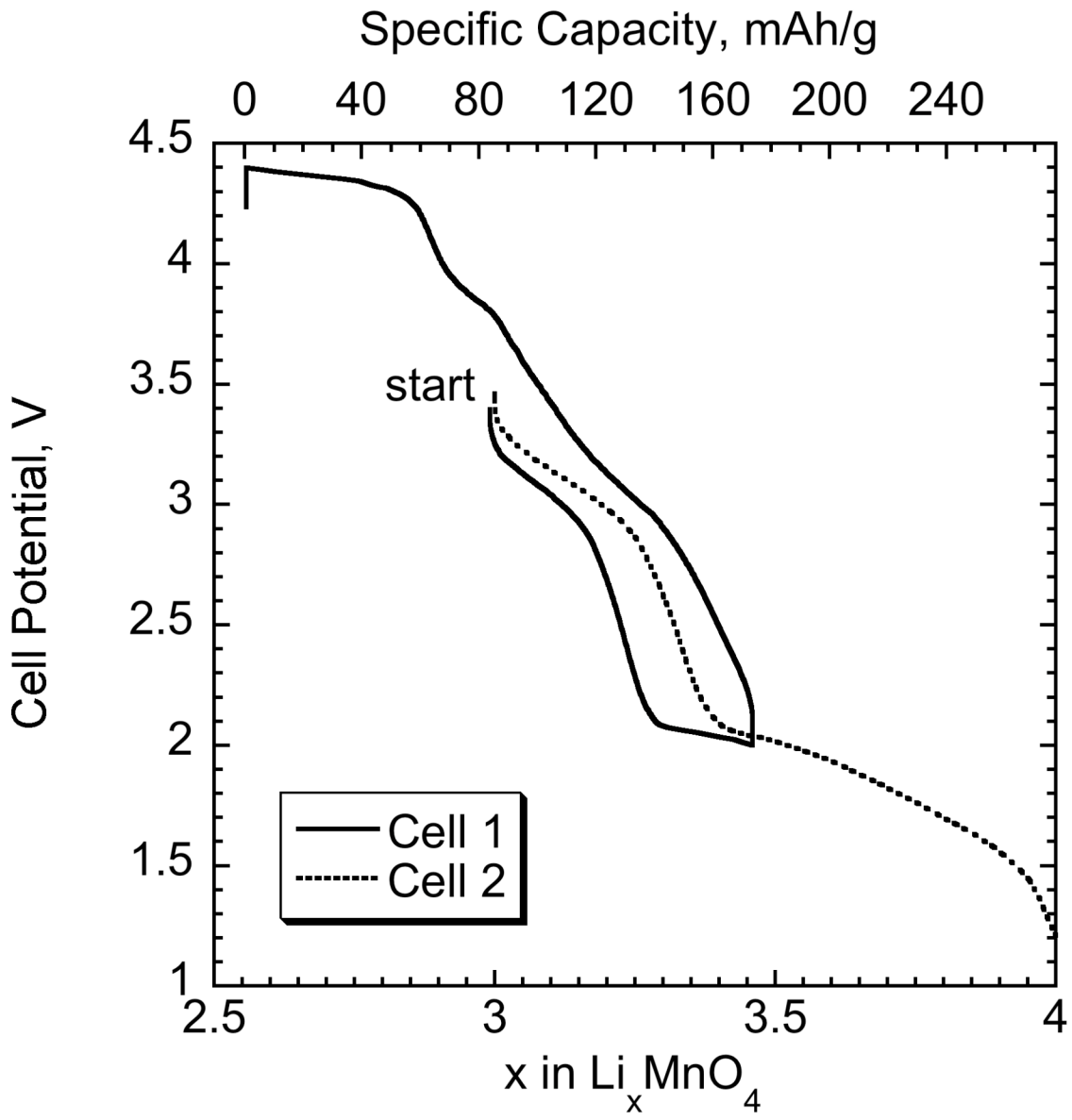
Specific Capacity, mAh/g
0
40
80
120
160
200
240
4.5
4
3.5
3
2.5
2
1.5
1
Cell Potential, V
start
Cell 1
Cell 2
2.5
3
3.5
4
x in Li x MnO 4

Figure 7

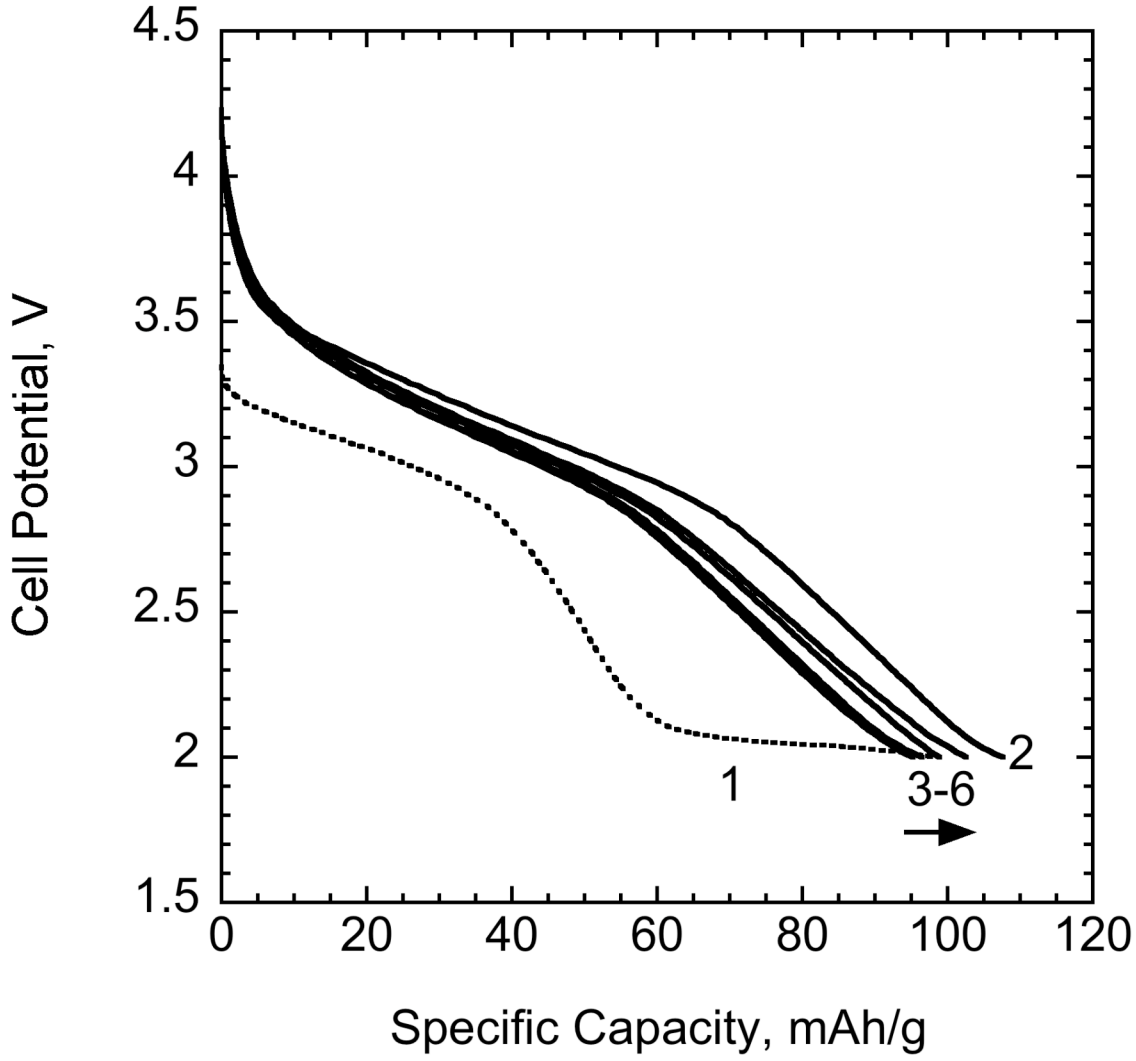
4.5
4
3.5
3
2.5
2
1.5
Cell Potential, V
0
20
40
60
80
100
120
Specific Capacity, mAh/g
1
2
3-6

Figure 8

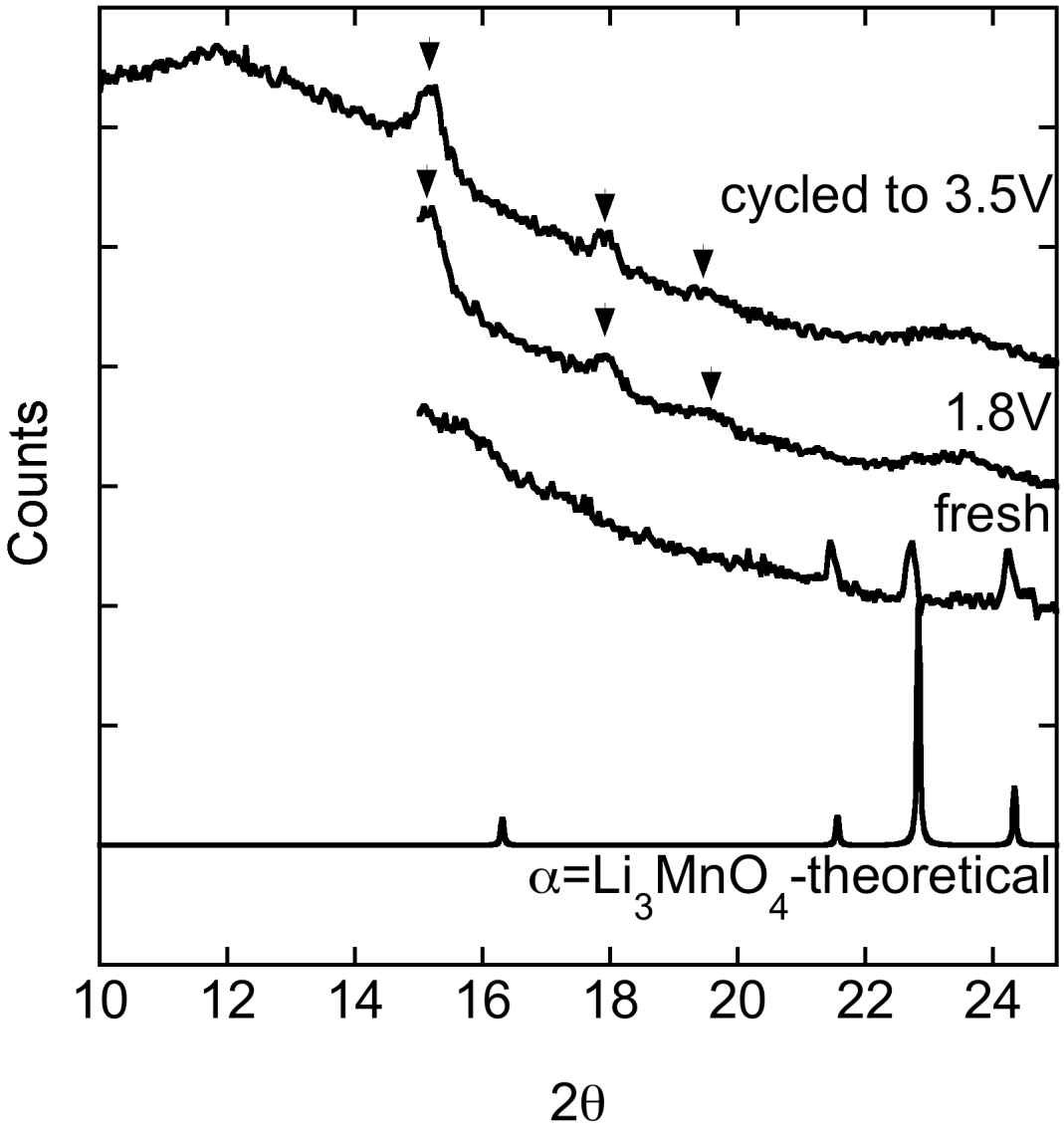
cycled to 3.5V
1.8V
fresh
α=Li3MnO4-theoretical
Counts
10
12
14
16
18
20
22
24
2θ

Figure 9

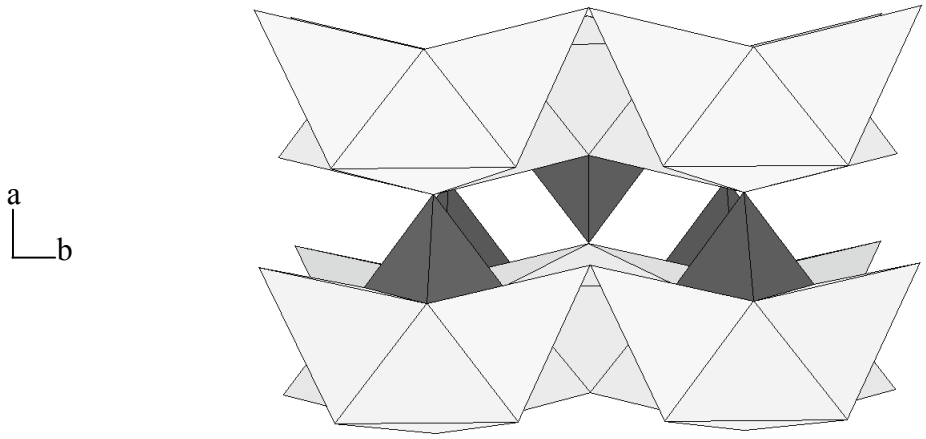

(a)

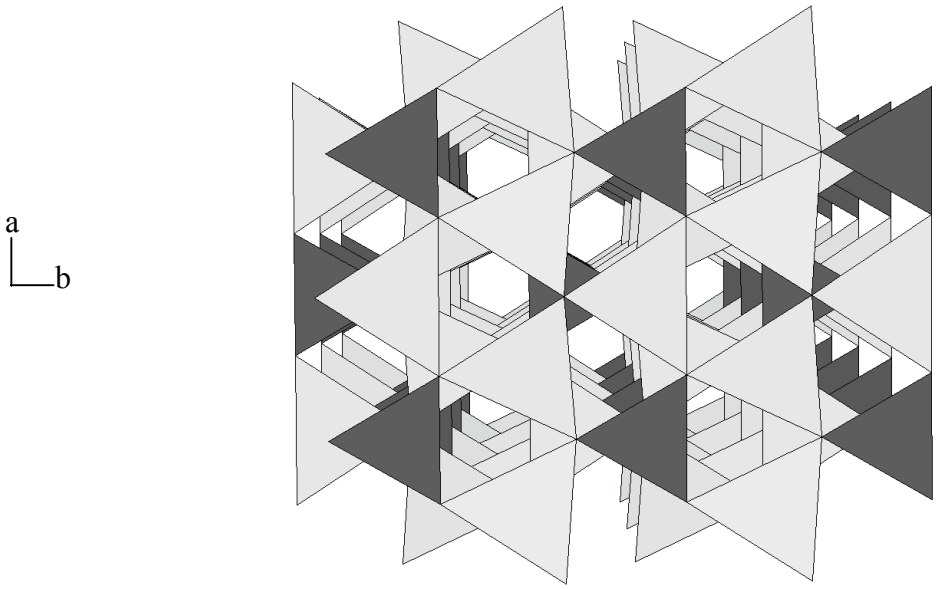

(b)

Figure 10